Electronic Supplementary Information for

Hand-gesture recognition using self-powered and single-electrode motion sensors fabricated with InN nanowires

Jaehyeok Shin,[a] Seunghwan Jhee,[a] Sumin Kang,[a] Hye Min Oh,[b] Chang Kyu Jeong,[c] Siyun Noh[d] and Jin Soo Kim[*a]

[a]Department of Electronic and Information Materials Engineering, Division of Advanced Materials Engineering, Research Institute of Materials and Energy Science, and Research Center of Advanced Materials Development, Jeonbuk National University, Jeonju 54896, Republic of Korea

[b]Department of Physics, Kunsan National University, Gunsan 54150, Republic Korea

[c]Department of Energy Storage and Conversion Engineering of Graduate School and Hydrogen and Fuel Cell Research Center, Jeonbuk National University, Jeonju 54896, Republic of Korea

[d]Department of Electrical and Computer Engineering, The Ohio State University, Columbus, Ohio, 43210, USA

[*]Author to whom any correspondence should be addressed.
E-mail: kjinsoo@jbnu.ac.kr

Formation of the highly crystalline InN NWs

Fig. S1 shows a schematic illustration of the formation of the InN NWs using the so-called In pre-deposition method. Prior to the formation of the InN NWs, the Si(111) substrate was chemically precleaned in a $HCl:H_2O_2:H_2O$ solution. After the precleaning process, the native oxidation layer that naturally formed on the Si(111) substrate was removed with the aid of *in situ* thermal annealing at 900 °C for 1 hour (deoxidation process). Subsequently, In droplets were deposited to serve as the initial nucleation sites for the subsequent growth of InN NWs by supplying only In with a beam equivalent pressure of 4.2×10^{-8} torr. After the formation of these droplets, In and N-plasma fluxes were simultaneously supplied to form the InN NWs. The additionally supplied In and N adatoms migrate to the In droplets where they crystallize into InN NWs. The detailed growth conditions for InN NWs are described in our previous papers.[1,2]

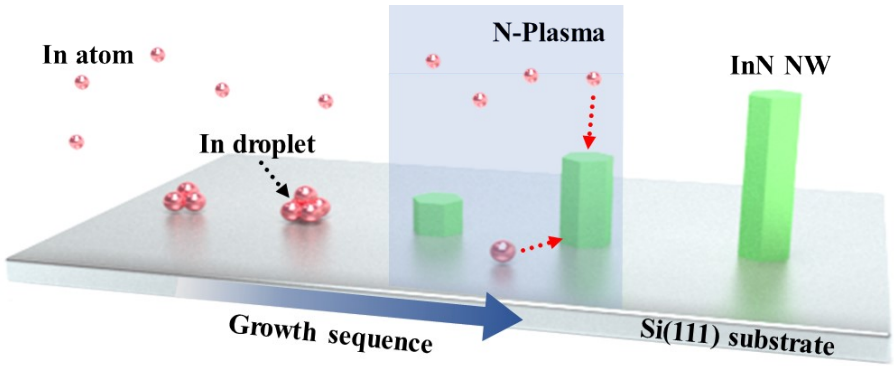

Fig. S1 Schematic diagram of the formation of InN NWs using the In pre-deposition method.

Structural characterizations of the InN NWs

Fig. S2a shows a cross-sectional FE-SEM image of the InN NWs formed on the Si(111) substrate. The average length and diameter of the InN NWs were measured to be 1213±2 and 76±0.8 nm, respectively. The InN NWs have a slightly tapered shape due to the nitrogen blocking effect, which limits the vertical migration of In atoms under N-rich conditions.[3] The inset shows the plan-view FE-SEM image of the InN NWs in which the hexagonal-shaped surfaces are clearly observed, indicating that the InN NWs were formed with the WZ crystal structure. The DCXRD patterns of the InN NWs (Fig. S2b) exhibit two peaks at 31.2 and 65.1°, which correspond to the (0002) and (0004) reflections for the WZ crystal structure of InN. Reflections related to any of the other planes were not observed, indicating that the InN NWs were grown along the c-axis without the formation of polycrystalline layers.[4] The full-width at half-maximum (FWHM) values of the (0002) and (0004) reflections of the InN were calculated to be 0.35 and 0.33°, respectively, which are much narrower than those of previously reported results.[5,6] The Raman spectrum of the InN NWs (Fig. S2c) has distinct active phonon modes at approximately 88, 439, 488, 516, and 589 cm^{-1}, corresponding to the E_2(low), A_1(TO), E_2(high), Si, and A_1(LO), respectively. These results are in good agreement with those in previous reports on InN with the WZ crystal structure.[7,8] The FWHM value of the E_2(high) peak was measured to be 12.1 cm^{-1}, which, upon application of bi-axial strain to the InN NWs, would typically broaden into an asymmetric shape. However, in our work, the E_2(high) peak had a symmetric shape with a small FWHM value, indicating that the bi-axial strain in the InN NWs is negligible.[7] Fig. S2d shows cross-sectional (left) and high-resolution (middle) TEM (HR-TEM) images of an individual InN NW, and the selective-area electron diffraction (SAED) patterns measured at two different positions on the InN NW along the vertical growth direction. For TEM analysis, InN NW samples were immersed in IPA for mechanical and ultrasonic agitation to form a suspension of NWs in IPA. Subsequently, a small drop of the

NW-IPA suspension was dropped onto a carbon-coated copper grid and dried under ambient conditions. From the HR-TEM images, the interplanar distance was measured to be 0.29 nm, which corresponds to the (002) lattice plane of InN with the WZ crystal structure.[9] In addition, stacking faults, common in Si-based III-V NWs because of the differences in the parameters of the two materials, were not obvious.[10,11] The SAED patterns clearly displayed the [0002] and [01-10] reflections of InN with the WZ crystal structure. The EDS mapping images (Fig. S2e) indicate the homogeneous distribution of elemental In and N throughout the InN NW. The EDS survey spectrum of the InN NWs, which appears in Fig. S2f, shows that only the expected elements In and N are present. The inset shows the weight and atomic percentages of each element, which confirm that the InN NW was formed stoichiometrically.

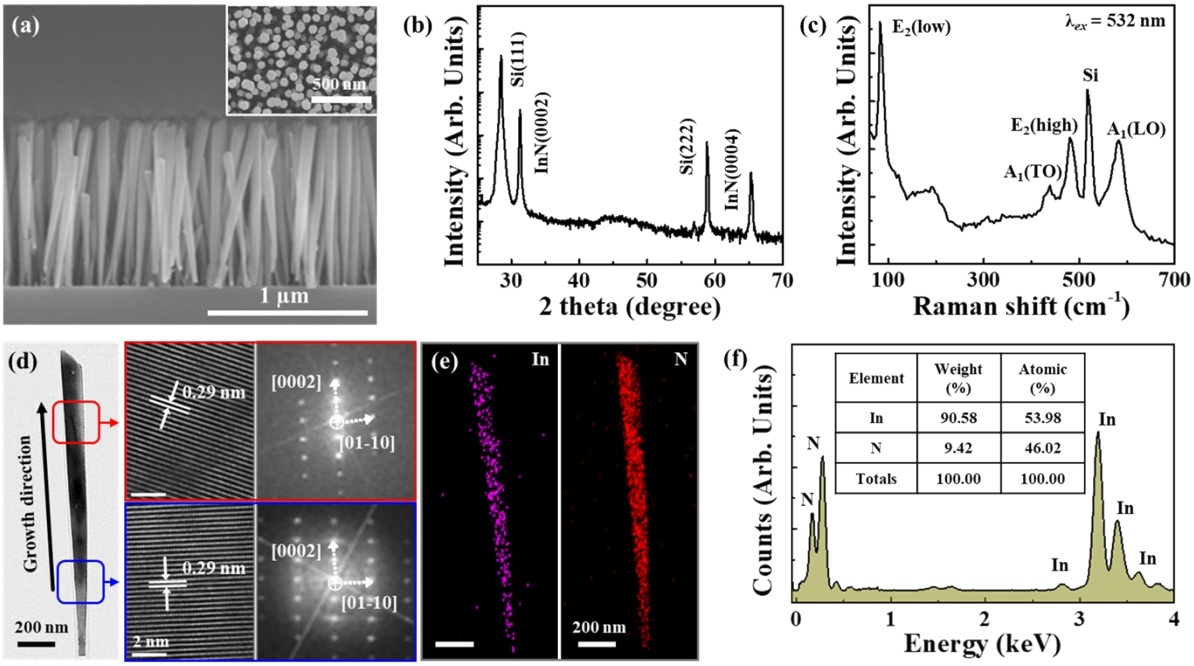

Fig. S2 (a) Cross-sectional and plan-view (inset) FE-SEM images of the InN NWs. (b) DCXRD curve of the InN NWs. (c) Raman spectrum of the InN NWs. (d) TEM (left), HR-TEM (middle), and SAED pattern (right) images measured at two different vertical positions. (e) EDS mapping images of the InN NW, showing the distribution of In (purple) and N (red). (f) EDS spectrum of the InN NWs, where the inset shows the summary on the weight and atomic percentage of each element.

Evaluation of the piezoelectric property of the InN NWs

The piezoelectric properties of the InN NWs were investigated using piezoresponse force microscopy (PFM) in the out-of-plane mode, implemented in a commercially available atomic force microscopy (AFM, Park Systems NX10) system. Fig. S3a and b show the surface morphology and PFM amplitude mapping image of an InN NW, respectively. The frequency and amplitude of the driving voltage were 17 kHz and 8 V, respectively. The piezoelectric coefficient was estimated to be 7.5 pm/V, which is in good agreement with the previously reported result.[12] The PFM amplitude of the NW is higher than that of the background electrode, indicating that forward deformation of the NW has taken place.[13] Fig. S3c shows the PFM phase-mapping image of the InN NW. A clear phase contrast is observed along the NW, indicating the formation of a well-defined piezoelectric domain and the active polarization response of the InN NW under the applied electric field. From these results, we can conclude that, owing to their piezoelectric properties, the InN NWs are an effective response medium for the PMS.

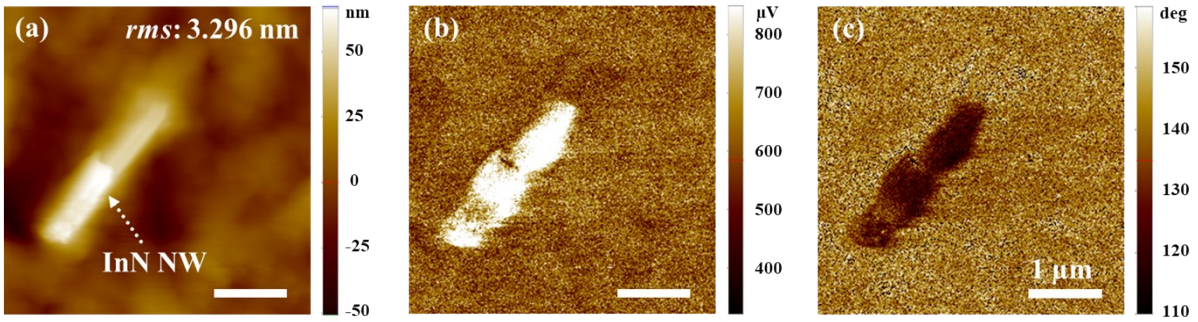

Fig. S3 (a) Surface morphology, (b) PFM amplitude, and (c) phase-mapping images of the InN NW.

Magnetic characterization of the InN NWs

Fig. S4a shows the magnetization curves of the PET substrate and InN NWs/PET. The expanded plot of the magnetization curves is also shown in Fig. S4b. The PET substrate without InN NWs exhibited a negligibly small magnetic signal. However, the InN NWs/PET showed a distinct magnetic response with a remanent magnetization of 8.86 memu/g. The magnetic behavior of InN NWs is largely related with the high surface-to-volume ratio and surface defects such as dangling bonds and vacancies.[14-16]

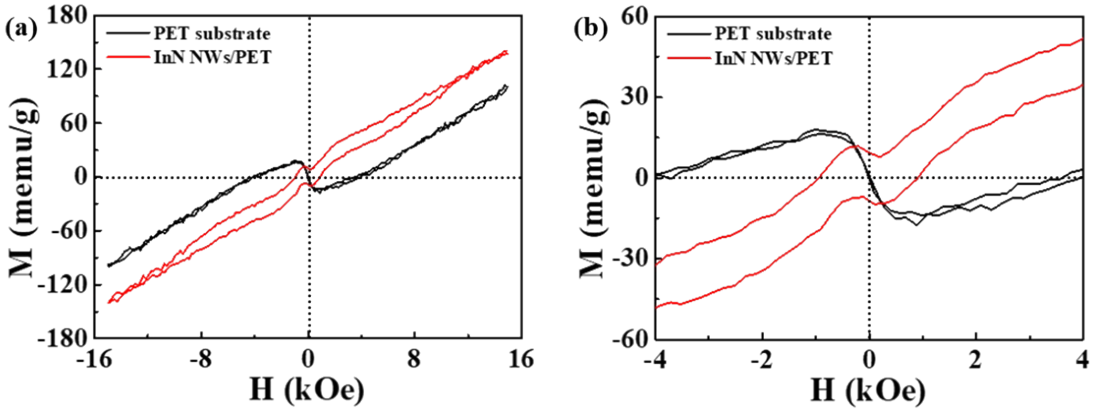

Fig. S4 (a) Magnetization curves of the PET substrate and InN NWs/PET and (b) expanded plot in the range of -4 to 4 kOe.

Evaluation of the magnetic alignment characteristics of the InN NWs

Fig. S5a-f present magnified plan-view FE-SEM images of the aligned InN NWs at magnetic field strengths of 0, 10, 20, 30, 40, and 50 G, respectively. As the magnetic strength increased, the degree of alignment of the NWs improved such that a magnetic field strength greater than the threshold value of 40 G proved sufficient to align the InN NWs along the direction of the magnetic field. The application of 50 G ensured that the InN NWs were completely aligned along the direction of the applied magnetic field. Fig. S5g presents a large-area plan-view FE-SEM image of the magnetically aligned InN NWs at the magnetic field of 50 G, clearly revealing their orientation along the magnetic-field direction.

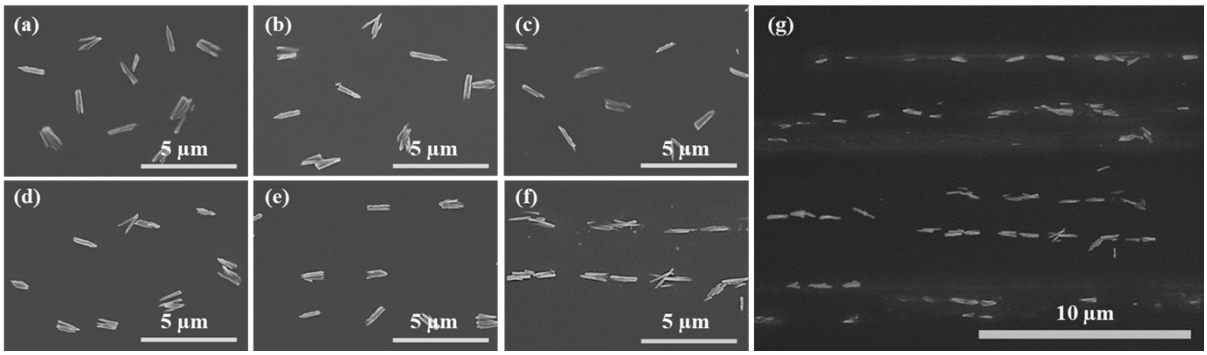

Fig. S5 Magnified plan-view FE-SEM images of the aligned InN NWs at different magnetic field strengths: (a) 0, (b) 10, (c) 20, (d) 30, (e) 40, and (f) 50 G. (g) Large-area plan-view FE-SEM image of the magnetically aligned InN NWs at the magnetic field of 50 G.

Calculation of the strength of the magnetic field inside the solenoid coil

The interior of the solenoid coil is schematically illustrated in Fig. S6. The strength of the magnetic field inside the solenoid coil can be calculated by the following equation.

$$H = \frac{4\pi ni}{10L}\left[\frac{L+2x}{\sqrt{2D^2+(L+2x)^2}} + \frac{L-2x}{\sqrt{2D^2+(L-2x)^2}}\right] \quad (1)$$

where the *n* is the number of coils wound, *D* is the diameter of the solenoid coil, *L* is the length of the solenoid coil, *i* is the applied current, and *x* is the distance between the center position and specific position inside the solenoid coil, respectively. The magnetic field strength applied to the sample of InN NWs at the center of the solenoid coil was systematically controlled by varying the current.

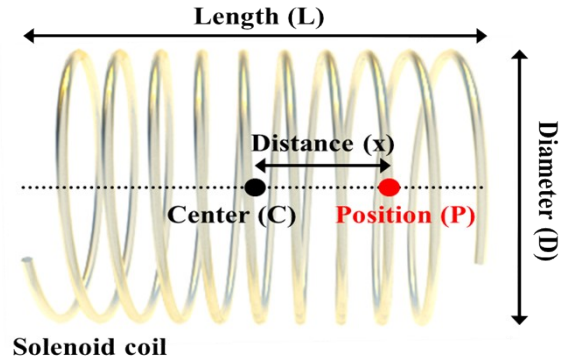

Fig. S6 Schematic diagram of the inside of the solenoid coil.

Raman spectra of the graphene with a different number of stacking layers

Fig. S7 shows the Raman spectra of the graphene with a different number of stacking layers without InN NWs. To avoid damage to the graphene during Raman measurements, a low excitation power setting (1 mW) was used for the laser with an operating wavelength of 532 nm (2.33 eV). The intensity of the D peak, typically positioned at approximately 1355 cm^{-1}, was very low such that it was rarely detected, indicating that the graphene was highly crystalline with few defects.[17] The two main pronounced peaks were those at 1586 cm^{-1} for the G peak and 2683 cm^{-1} for the 2D peak. The G and 2D peaks originate from the in-plane vibration of sp^2 carbon atoms corresponding to the doubly degenerate (TO and LO) phonon mode (E_{2g} symmetry) at the center of the Brillouin zone and a two-phonon double resonance Raman process, respectively.[18,19] The intensity ratio (I_G/I_{2D}), the ratio of the intensity of the G peak to that of the 2D peak, of single- to sextuple-layer graphene was calculated to be 0.41, 0.62, 0.85, 1.14, 1.75, and 2.34, respectively. The 2D peak retained a symmetric shape throughout, and the FWHM value increased slightly to 33.7, 35.2, 36.8, 41.2, 48.9, and 50.3 cm^{-1}. These results are characteristic of turbostratic graphene in which interlayer coupling is suppressed due to rotational misalignment between layers.[20-22] In such structures, each graphene layer contributes independently to the Raman scattering and behaves similarly to single-layer graphene. As a result, due to the incomplete overlap of individual layers, the intensity of the 2D peak decreases linearly with the number of layers, while the peak position does not change significantly. The slight broadening of the 2D peak can be attributed to local variations in the stacking angle or inhomogeneities induced by residual strain.[23]

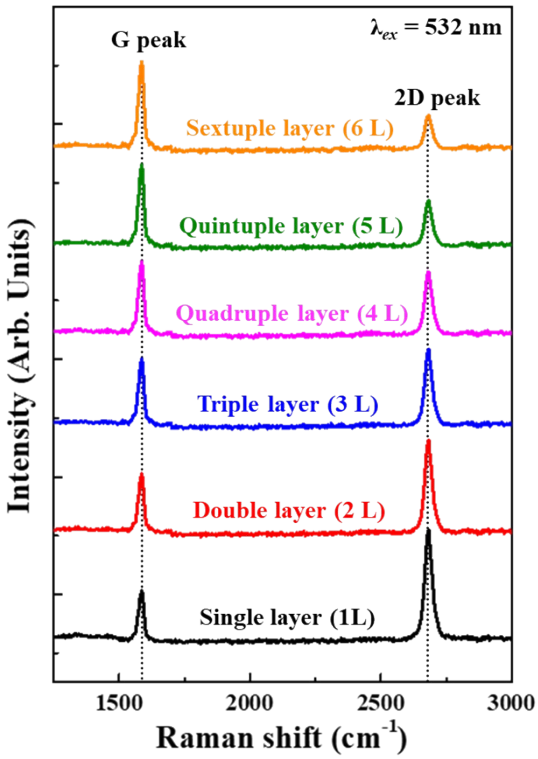

Fig. S7 Raman spectra of graphene layers transferred onto the PET substrate.

Evaluation of the flexibility and durability of the graphene channel

The sheet resistance of the quintuple graphene layer with respect to the number of bending cycles is plotted in Fig. S8. After 500 cyclic-bending tests, the sheet resistance deviated negligibly from its initial value. Based on this result, we concluded that the graphene channel exhibits excellent durability.

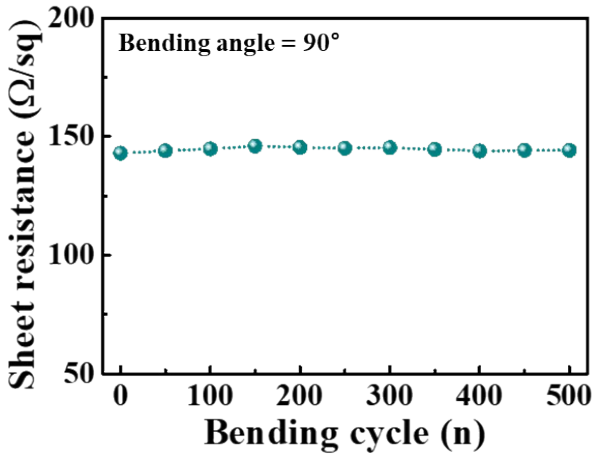

Fig. S8 Summary of the sheet resistance of the graphene channel with respect to the number of bending cycles.

Effect of the number of graphene layers on the device performance

Fig. S9 shows the schematic illustration for the effect of the number of graphene layers on the device performance. With increasing the number of graphene layers, the electrical resistance of the graphene channel is significantly reduced, which facilitates more efficient charge collection and transfer. This improvement in electrical conductivity minimizes internal losses, thereby enhancing the piezoelectric potential and leading to a higher output voltage.

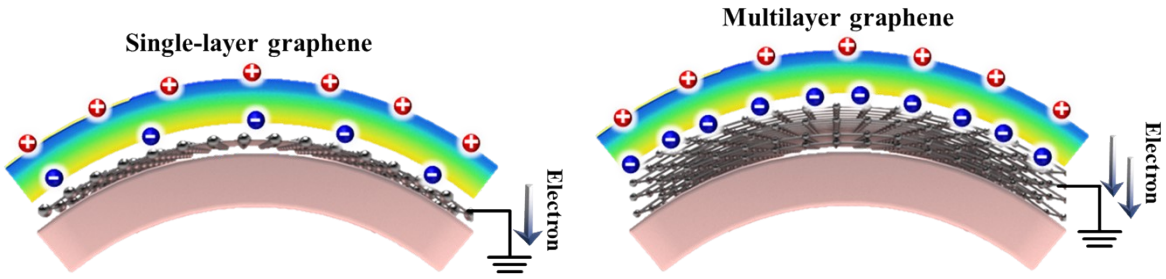

Fig. S9 Schematic illustration for the effect of the number of graphene layers on the device performance.

FE-SEM images of InN NWs different lengths

Fig. S10 shows cross-sectional FE-SEM images of the InN NWs with the average lengths of (a) 403, (b) 651, (c) 811, (d) 970, (e) 1213, and (f) 1398 nm. The length of the InN NWs was adjusted by varying the growth time.

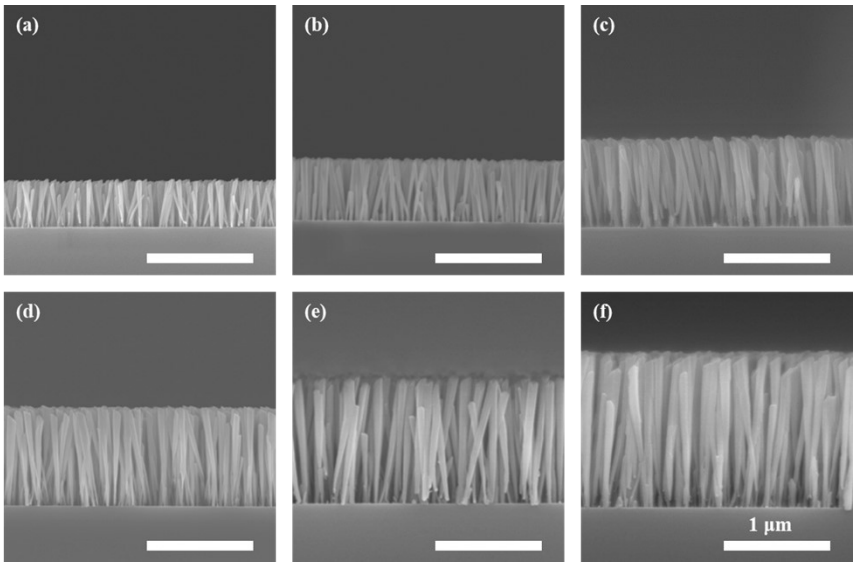

Fig. S10 Cross-sectional FE-SEM images of InN NWs with the average length of (a) 403, (b) 651, (c) 811, (d) 970, (e) 1213, and (f) 1398 nm.

Evaluation of the cross-talk and synchronization between adjacent chips

Fig. S11 shows the output voltage signals measured from two PMSs individually attached to the DIP and PIP joints of the index finger while grasping a baseball. Two sensors simultaneously produced distinct signal corresponding to their deformation depending on the motion of finger joints. When grasping the baseball, the DIP and PIP joints were bent by approximately 30 and 40°, respectively, and the corresponding output voltages were measured to be 3.47 and 4.36 V, respectively. This result clearly demonstrates that each sensor responds independently to the mechanical deformation of its respective finger joint without noticeable interference or cross-talk between chips.

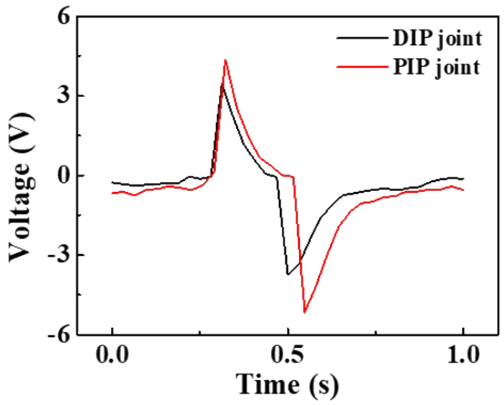

Fig. S11 Output-voltage curves of the two PMSs individually attached to the DIP and PIP joints of the index finger while grasping a baseball.

References

[1] J. Shin, S. Noh, J. Lee, J. Oh, M.-Y. Ryu and J. S. Kim, *Appl. Sci. Converg. Technol.*, 2022, **31**, 141-144.

[2] J. Shin, H. Yang, S. Noh, S. Han and J. S. Kim, *Nanoscale*, 2022, **14**, 10793-10800.

[3] F. Gao, L. Wen, Z. Xu, J. Han, Y. Yu, S. Zhang and G. Li, *Small*, 2017, **13**, 1603775.

[4] A. Wierzbicka, G. Tchutchulashvili, M. Sobanska, K. Kloser, R. Minikayev, J. Z. Domagala, J. Borysiuk and Z. R. Zytkiewicz, *Appl. Surf. Sci.*, 2017, **425**, 1014-1019.

[5] A. O. Ajagunna, E. Iliopoulos, G. Tsiakatouras, K. Tsagaraki, M. Androulidaki and A. Georgakilas, *J. Appl. Phys.*, 2010, **107**, 024506.

[6] M. Zeghouane, G. Avit, T. W. Cornelius, D. Salomon, Y. André, C. Bougerol, T. Taliercio, A. Meguekam-Sado, P. Ferret, D. Castelluci, E. Gil, E. Tournié, O. Thomas and A. Trassoudaine, *CrystEngComm.*, 2019, **21**, 2702-2708.

[7] K. K. Madapu, A. K. Prasad, A. K. Tyagi and S. Dhara, *AIP Conf. Proc.*, 2015, **1665**, 050089.

[8] S. Alkis, F. I. Chowdhury, M. Alevli, N. Dietz, B. Yalizay, S. Aktürk, A. Nayfeh and A. K. Okyay, *J. Opt.*, 2015, **17**, 105903.

[9] H. Li, G. Zhao, L. Wang, Z. Chen and S. Yang, *Nanomaterials*, 2016, **6**, 195.

[10] S. Eftychis, J. Kruse, T. Koukoula, Th. Kehagias, Ph. Komninou, A. Adikimenakis, K. Tsagaraki, M. Androulidaki, P. Tzanetakis, E. Iliopoulos and A. Georgakilas, *J. Cryst. Growth.*, 2016, **442**, 8-13.

[11] R. S. Chen, H. Y. Tsai, C. H. Chan, Y. S. Huang, Y. T. Chen, K. H. Chen and L. C. Chen, *J. Electron. Mater.*, 2015, **44**, 177-187.

[12] F. Bernardini and V. Fiorentini, *Appl. Phys. Lett.*, 2002, **80**, 4145-4147.

[13] S. Wu, J. Zhang, X. Liu, S. Lv, R. Gao, W. Cai, F. Wang and C. Fu, *Nanomaterials*, 2019, **9**, 190.

[14] O. Y. Xie, M. Q. Gu, L. Huang, F. M. Zhang and X. S. Wu, *AIP Adv.*, 2012, **2**, 012185.

[15] M. Farzan, S. M. Elahi, M. R. Abolhassani and H. Salehi, *Superlattices Microstruct.*, 2017, **105**, 99-109.

[16] B. Song, K. Zhu, J. Liu, J. Jian, J. Han, H. Bao, H. Li, Y. Liu, H. Zuo, W. Wang, G. Wang, X.

Zhang, S. Meng, W. Wang and X. Chen, *J. Mater. Chem.*, 2010, **20**, 9935-9940.

[17] E. S. Roscher, R. Hoffmann and O. Ambacher, *Anal. Methods.*, 2019, **11**, 1224-1228.

[18] Z. Ni, Y. Wang, T. Yu and Z. Shen, *Nano Res.*, 2008, **1**, 273-291.

[19] C. Thomsen and S. Reich, *Phys. Rev. Lett.*, 2000, **85**, 5214.

[20] Z. Wang, H. Ogata, S. Morimoto, M. Fujishige, K. Takeuchi, H. Muramatsu, T. Hayashi, J. Ortiz-Medina, M. Z. M. Yusop, M. Tanemura, M. Terrones, Y. Hashimoto and M. Endo, *J. Mater. Chem. A.*, 2015, **3**, 14545-14549.

[21] M. Gautam, Z. Shi and A. H. Jayatissa, *Sol. Energy Mater. Sol. Cells.*, 2017, **163**, 1-8.

[22] J. Berashevich and T. Chakraborty, *Phys. Rev.*, 2011, **84**, 033403.

[23] A. H. Alami, K. Aokal, D. Zhang and B. Soudan, *Appl. Nanosci.*, 2018, **8**, 1943-1950.